UC Berkeley
UC Berkeley Previously Published Works

Title
Deformation and failure of the CrCoNi medium-entropy alloy subjected to extreme shock loading

Permalink
https://escholarship.org/uc/item/9kg339m2

Journal
Science Advances, 9(18)

ISSN
2375-2548

Authors
Zhao, Shiteng
Yin, Sheng
Liang, Xiao
et al.

Publication Date
2023-05-05

DOI
10.1126/sciadv.adf8602

Peer reviewed

MATERIALS SCIENCE

Deformation and failure of the CrCoNi medium-entropy alloy subjected to extreme shock loading

Shiteng Zhao[1,2]†*, Sheng Yin[3]†, Xiao Liang[1], Fuhua Cao[4], Qin Yu[3], Ruopeng Zhang[5], Lanhong Dai[4], Carlos J. Ruestes[6,7], Robert O. Ritchie[3,8], Andrew M. Minor[5,8]*

The extraordinary work hardening ability and fracture toughness of the face-centered cubic (fcc) high-entropy alloys render them ideal candidates for many structural applications. Here, the deformation and failure mechanisms of an equiatomic CrCoNi medium-entropyalloy (MEA) were investigated by powerful laser-driven shock experiments. Multiscale characterization demonstrates that profuse planar defects including stacking faults, nanotwins, and hexagonal nanolamella were generated during shock compression, forming a three-dimensional network. During shock release, the MEA fractured by strong tensile deformation and numerous voids was observed in the vicinity of the fracture plane. High defect populations, nanorecrystallization, and amorphization were found adjacent to these areas of localized deformation. Molecular dynamics simulations corroborate the experimental results and suggest that deformation-induced defects formed before void nucleation govern the geometry of void growth and delay their coalescence. Our results indicate that the CrCoNi-based alloys are impact resistant, damage tolerant, and potentially suitable in applications under extreme conditions.

INTRODUCTION

The need for high-performance structural materials that can be effective under extreme conditions is one of the outstanding technological challenges in materials science. To meet this challenge, materials need to be developed that not only have higher strength and toughness but also can retain these characteristics at elevated temperatures or strain rates. The emerging concept of multiple principal element alloys, often termed high- or medium-entropy alloys (HEA/MEAs), provides these opportunities (1–11). In particular, CrCoNi-based HEA/MEAs and their variants exhibit remarkable fracture toughness and damage tolerance over ambient-to-cryogenic temperatures due to continuous strain hardening induced by a sequence of plastic deformation mechanisms, particularly a strong effect of twinning and transformation-induced plasticity (TWIP and TRIP) (12–17). Because twinning is also promoted by elevated strain rates (>10^3/s), the mechanical properties of these alloys are expected to excel under extreme impact or shock conditions. Recent studies in pristine CrCoNi-based HEA/MEAs have revealed a remarkable resistance to shear localization under dynamic loading in a strain rate of ~10^3/s (18, 19). For example, Yang et al. (20) reported that microstructurally tailored HEA/MEAs displayed a higher strength at high strain rates with twinning acting to suppress shear banding (21). Yang et al. (22) investigated the dynamic tension of the $Fe_{40}Mn_{20}Cr_{20}Ni_{20}$ HEA and showed that strength, tensile ductility, and strain rate sensitivity were all improved at the elevated strain rates. Jiang et al. (23) first investigated the shock deformation of the CrMnFeCoNi HEA using a single-stage gas gun and suggested that the alloy displayed a reasonably high strength at a strain rate of ~10^6/s. It was also found that hydrogen can delay the spall failure of this alloy (24). Zhang et al. (25) recently studied the spallation, i.e., failure of materials under dynamic tensile loads, of the $Al_{0.1}CoCrFeNi$ HEA using a plate impact technique and suggested that the material can display a high spall strength (up to 4 GPa) with marked strain rate sensitivity. Microstructurally, HEA/MEAs in general exhibit extremely versatile deformation mechanisms at elevated strain rates, including dislocation-mediated plasticity, twinning, phase transition, and, in extreme, solid-state amorphization (26). These promising results suggest that the CrCoNi-based alloys are potential candidates for applications in extreme conditions. However, there is still little information concerning the behavior of these materials under very high strain rate exceeding 10^6/s, where a strong shock wave is created in the deformed body.

The failure of ductile metals under extreme tensile loading conditions usually involves a cavitation instability, which involves the nucleation, growth, and coalescence of voids (27). Compared with behavior under quasi-static loading, cavitation under dynamic loading is complicated by additional coupling mechanisms, including strain rate hardening (28), adiabatic heating (29), thermal softening (30), and inertia effects (31). Huang et al. (32) pointed out that the competition between these effects can lead to various void growth characteristics. There have been intense theoretical, computational, and experimental efforts over the past decades to understand these phenomena (33–38). It is relatively well accepted that the nucleation of voids is highly anisotropic and extremely microstructure sensitive (39–41). Specifically, grain boundaries are considered as the "weak spots" as they provide preferred nucleation cites for voids (42, 43). The spall strength of polycrystalline metals is therefore lower than their monocrystalline counterparts (40). Subsequent void growth is essentially a plasticity-induced mass transportation process, which in metals involves the emission of defects from the surface of the cavities (33, 44). Voids impingement occurs

[1]School of Materials Science and Engineering, Beihang University, Beijing, China. [2]Tianmushan Laboratory, Xixi Octagon City, Hangzhou, China. [3]Materials Sciences Division, Lawrence Berkeley National Laboratory, Berkeley, USA. [4]Institute of Mechanics, Chinese Academy of Sciences, Beijing, China. [5]National Center for Electron Microscopy, Molecular Foundry, Lawrence Berkeley National Laboratory, Berkeley, CA, USA. [6]IMDEA Materials Institute, Calle Eric Kandel 2, Getafe, 28906 Madrid, Spain. [7]Instituto Interdisciplinario de Ciencias Básicas (ICB), CONICET UNCUYO, Padre J. Contreras 1300, 5500 Mendoza, Argentina. [8]Department of Materials Science and Engineering, UC Berkeley, Berkeley, CA, USA.
*Corresponding author. Email: szhao@buaa.edu.cn (S.Z.); aminor@berkeley.edu (A. M.M.)
†These authors contributed equally to this work.

once an individual cavity grows into the adjacent ones to form the fracture surface, although the process is markedly facilitated by shear localization between the voids, which can, in extreme cases, lead to catastrophic failure (45). However, despite this understanding of dynamic failure, the detailed microscopic mechanisms, particularly the linkage between local microstructure and the dynamic behavior of materials, remain unclear. Recent molecular dynamics (MD) simulations indicate that the local chemical fluctuation can markedly affect both dislocation activities (46) and the void dynamics in HEAs (47) and, hence, influence their impact resistance. Further understanding of the underlying material physics would certainly aid the design of impact-resistant materials, which has been an ongoing challenge for many applications including vehicle crash safety, penetration protection, and aerospace engineering.

RESULTS AND DISCUSSION

The dynamic mechanical behavior of the CrCoNi MEA was evaluated in both compression and tension. Pulsed laser-driven experiments were used to subject targets to an extremely high degree of stress within a time frame of nanoseconds. The time-resolved free-surface velocity profile of the shocked sample was measured by a velocity interferometry system for any reflector (VISAR), as seen in Fig. 1A. To preserve the integrity of the sample while preventing the complication of multiple plastic wave interactions, the sample was designed in such a way that the shock wave would decay substantially by the time it reached the rear surface and caused a spall fracture in its close vicinity. Information was then extracted directly from the shock surface and the cross section adjacent to the spall plane. Accordingly, both compression-dominated (at the front surface) and tension-dominated (at the rear surface) microstructures could be characterized. Representative optical micrographs of the recovered front and rear surfaces are shown in Fig. 1 (B and C), respectively. A crater caused by shock compression can be seen in Fig. 1B, whereas a tension-induced "bubble" is apparent in Fig. 1C. The spall strength σ_{th} of the CrCoNi MEA was determined from the free-surface velocity profiles using the simplified acoustic method

$$\sigma_{th} = \frac{1}{2}\rho_0 c_b (u_{max} - u_{min})$$
(1)

where $\rho_0 = 8.47$ g/cm^3 is the density, $c_b = 4.67$ km/s is the bulk sound velocity of the MEA [measured by the authors using ultrasonic pulsed echo method (48)], and u_{max} and u_{min} are, respectively, the maximum (shock break-out) and first minimum velocity (pull-back) determined from the free-surface velocity profile (Fig. 1 and fig. S1). Note that the strain rate during the laser-shock experiments is not constant, considering the rapid decay of the stress waves and their complicated interaction. Nevertheless, the nominal strain rate $\dot{\varepsilon}$ can be estimated on the basis of the free-surface velocity profile, $\dot{\varepsilon} \approx \frac{u_{max} - u_{min}}{2\Delta t \cdot c_b}$, where Δt is the time between u_{max} and u_{min}. On the basis of Eq 1, the spall strength of the MEA was estimated to be approximately 9.8 GPa at a strain rate of ~1 × 10^7/s, which is close to other heavy metals loaded in similar conditions (40, 41).
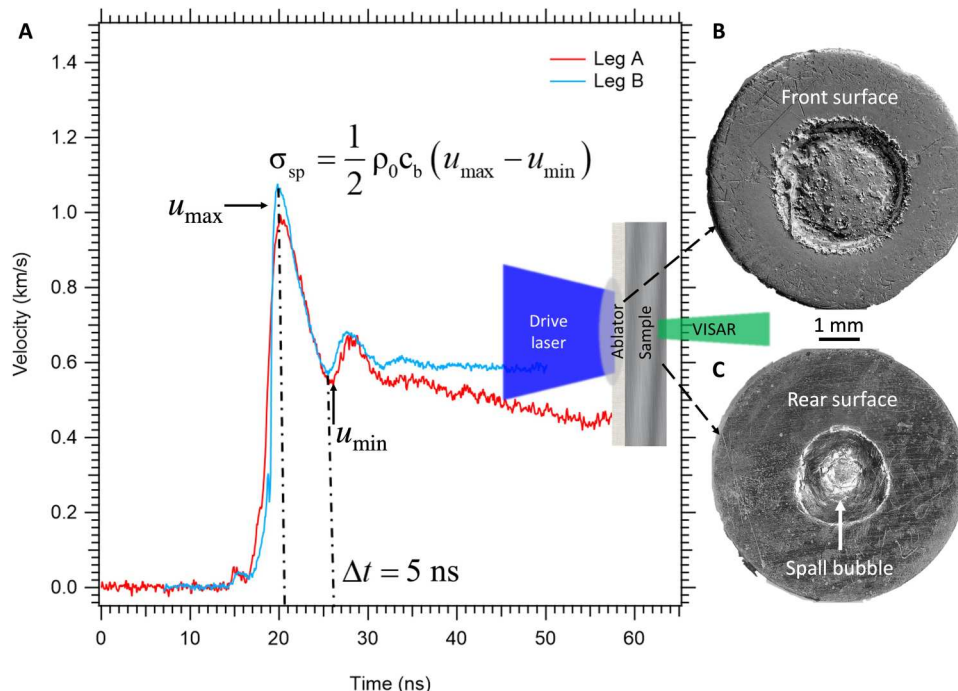

Fig. 1. Schematic drawing of the laser-shock experiments and free surface velocimetry of the target. (A) A polystyrene film was used as ablator to effectively convert laser energy into kinetic energy of the plasma, leading to a stress wave propagate into the sample. Two individual velocity interferometer systems for any reflector (VISAR) channels (leg A and B) were applied to unambiguously determine the free-surface velocity profile. The "pull-back" signal (u_{max}, u_{min}), which marks the wave reflection at the cavity surface, can be found in the profile, Δt is the time interval between u_{max} and u_{min}, and ρ_o and c_b are the initial density and bulk sound velocity of the material, respectively. **(B and C)** Front and rear surface of the laser shock–recovered target showing crater and spall bubble, respectively.

Dynamic compression

The microstructure after this extreme deformation was characterized by scanning transmission electron microscopy (STEM) of the laser shock–recovered target. The diffraction contrast STEM image in Fig. 2A reveals the overall picture, which consists of a high density of lattice defects lying mostly on the {111} planes. These defects are planar and are often intersected with each other, leading to a three-dimensional (3D) network. High-resolution STEM images in Fig. 2 (B to E) reveal the atomistic details of these deformation features, including stacking faults (Fig. 2B), Lomer-Cottrell locks (Fig. 2C), nanotwins (Fig. 2D), and hexagonal nanolamella (Fig. 2E). Such a diverse set of deformation mechanisms shown in the recovered sample suggests that the CrCoNi MEA can accumulate a remarkably high density of nanointerfaces during laser-shock compression. Such in situ formed nanointerfaces subsequently affect damage nucleation when a tensile wave impacts the material, the nature of which is discussed below.

3D defect network produced by shock compression

As shown in Fig. 2, the MEA deformed predominantly by planar faults under intense shock loading, which includes the generation of stacking faults, nanotwins, and hexagonal nanolamella. All these planar defects lie on the {111} slip planes of the lattice. This is, in part, due to the ultralow stacking fault energy (γ_{SFE}) of the CrCoNi alloy, because the critical stress for twin nucleation, $\sigma_{twin} \approx \frac{\gamma_{SFE}}{b}$, decreases with γ_{SFE} (where b is the Burgers vector). When the sample is subjected to shock compression, a high density of planar defects can be generated and distributed homogeneously. This is consistent with the early dislocation model of the shock front where dislocations (partial dislocations in this case) nucleate homogeneously across the interface between compressed and undeformed material (39). Of particular note is the deformation-induced phase transition. Certain computational studies have indicated that the free energy between face-centered cubic (fcc) and hexagonal close-packed (hcp) lattice is small in the CrCoNi MEA at ambient temperatures (49), rendering the deformation-induced fcc-to-hcp phase transition feasible. While such a phase transition has been observed in the same material deformed at reduced temperatures (17, 50), it was also seen in the shock-recovered alloy, as this phase transition appears to be concomitant with the formation of stacking faults and deformation twins; this indicates a strong correlation between cryogenic deformation and high strain rate phenomena. These correlations can often be interpreted by the Zener-Hollomon relation, although systematic experiments at various temperatures and strain rates need to be conducted to quantitatively explore this relationship. The versatile intersections of these planar faults, shown in Fig. 2A, produce a complex network in 3D space. The low SFE also limits the recombination of partial dislocations and thus leads to a high defect accumulation rate. Consequently, a high work-hardening rate is expected. Nanoindentation measurements of the moderately laser-shocked sample indicates a substantial increase in hardness by 30% compared with the as-received material (fig. S2). It also suggests the potential application of laser shot peening for the surface modification of this alloy.

MD simulations of in situ computational microscopy were conducted to gain further insights into the high strain rate deformation mechanisms (51); details of the methodology of these simulations are described in Materials and Methods. As the initial shock wave propagates across the sample due to the high strain rate compression, multiple deformation pathways can be activated in the CrCoNi MEA, including a high density of dislocations, deformation twinning, nucleation of hcp lamella, and amorphization. In Fig. 3, we display the microstructures of a single-crystal MEA sample under shock wave loading through MD simulation. Figure 3A depicts the deformed structure after the shock wave runs across the sample during the compression stage ($t = 20$ ps), with a correspondingly high density of shock-induced defects, as extracted by the crystal analysis tool (CAT). Figure 3B presents the shock pressure profile corresponding to Fig. 3A, where the elastic wave and plastic wave typical of shock compression of condensed matter can be seen. Careful examination of the deformed microstructures revealed extended defect architectures, including 3D nanointerfaces consisting of stacking faults on multiple {111} planes, hcp lamella, and deformation twinning, as shown in Fig. 3C. In addition, multiple Lomer-Cottrell locks were found in the shocked sample as shown in Fig. 3C, consistent with our experimental high-angle annular dark-field (HAADF) STEM micrographs. Initial amorphous regions can be frequently observed at the intersections of multiple stacking faults, as highlighted in Fig. 3D. As the shock wave gets reflected at the back surface and the sample becomes subjected to a tensile state, void nucleation gets triggered, as shown in Fig. 3E ($t = 52.5$ ps). Void nucleation takes place in amorphous regions induced by a high concentration of intersections of the planar defects (Fig. 3F), which creates a high shear strain and shear strain gradient (Fig. 3G). Correlation of the longitudinal stresses, stacking faults, and deformation twinning reveals that voids nucleate in regions where conditions of both high defect density (both stacking faults and deformation twins) and maximum tensile stresses are met. The nucleation process is also
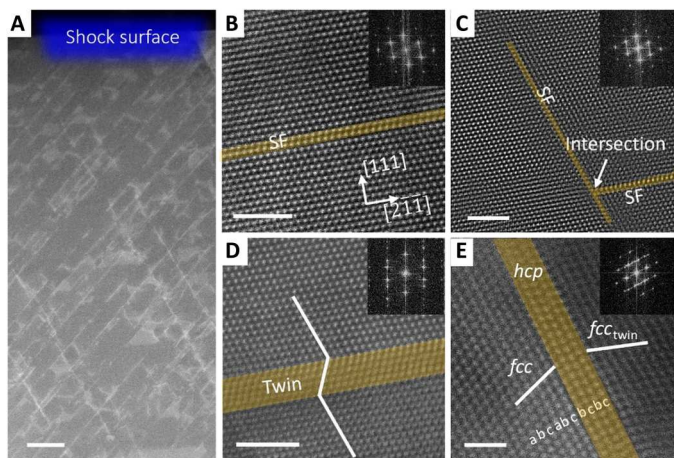
Fig. 2. Deformation microstructure of the shock-recovered CrCoNi MEA. (**A**) Diffraction contrast STEM imaging reveals a high density of the {111} defect networks produced by shock deformation. (**B**) Atomic-scale high-angle annular dark-field–STEM micrographs reveal that these defects are primarily stacking faults bonded by Shockley partial dislocations. SF, stacking fault. (**C**) Two leading Shockley partials on distinctive {111} planes often intersect and form immobile locks. (**D**) Propagation of Shockley partial dislocations on consecutive and alternating {111} planes leads to the formation of nanoscale twins (D) and hcp lamella (**E**), respectively. Scale bars, 200 nm (A), 2 nm (B) and (D), 5 nm (C), and 1 nm (E). All the TEM samples are taken from the shock surface (front surface) as shown schematically in Fig. 1B
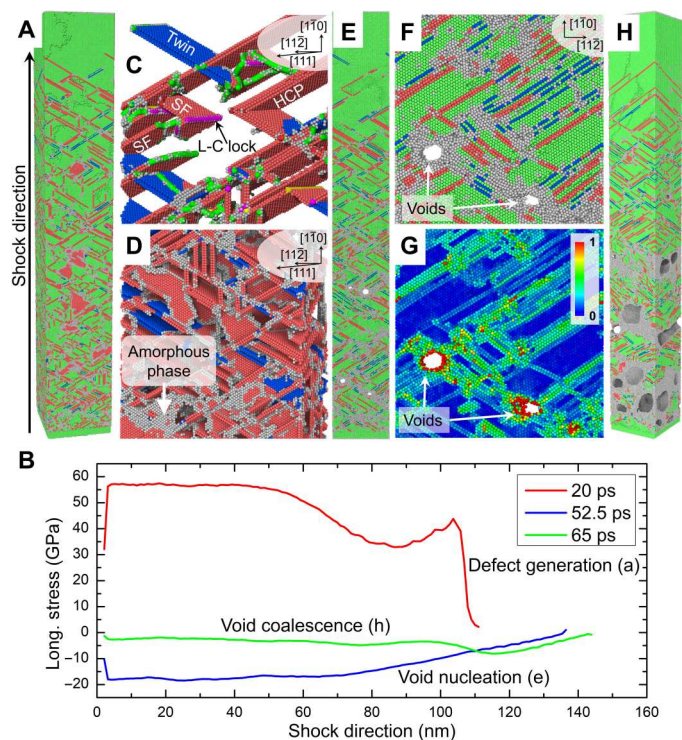
Fig. 3. Predicted microstructures in the CrCoNi MEA after the shock wave loading from MD simulations. (**A**) Microstructure after shock wave loading during the compression stage ($t = 20$ ps). The green represents fcc atoms, red represents hcp atoms, blue represents the twin boundary atoms, and gray represents amorphous atoms. (**B**) Longitudinal stress profiles for the initial defect generation (compression stage $t = 20$ ps), void nucleation ($t = 52.5$ ps), and coalescence ($t = 65$ ps). (**C**) 3D planar defects network. Only non-fcc atoms are shown and colored according to their defect classification, including stacking faults on multiple {111} planes, hcp lamella (HCP), and deformation twinning segments (twin). Several immobile Lomer-Cottrell (L-C) locks have also been observed in the sample. (**D**) Initial amorphous regions were frequently observed at the intersections of multiple stacking faults. (**E**) During the tensile condition, a high fraction of planar defects and amorphous regions are retained. (**F**) Voids nucleate in regions with amorphization, a high concentration of defects, and maximum tensile stresses [blue curve in (B)]. (**G**) Shear strain fields. The interaction of planar defects leads to high shear strains, inducing amorphization and void nucleation. (**H**) Spallation proceeds by void growth and coalescence, with substantial stress drop [green curve in (B)].

evident after triaxiality factor calculations (fig. S3). As the spallation process continues, voids grow and start to coalesce (Fig. 3H and movie S1).

Dynamic tension

When the stress wave is reflected at the free surface, the state of stress is reversed into tension to satisfy the traction-free boundary condition. This tensile stress, once above a certain threshold, leads to catastrophic failure of ductile materials by void nucleation, growth, and coalescence. We investigated these dynamic failure mechanisms in the CrCoNi MEA using multiscale electron microscopy. The morphological features and the local microstructure of the voids can be visualized by electron backscatter diffraction (EBSD) techniques. Figure 4 (A and B) illustrates the deformation microstructure adjacent to the voids where the EBSD map (orientation map overlaid with image quality map) shows the dark-contrasted slip traces.

Maps of the geometrically necessary dislocations (GNDs) in Fig. 4 (C and D) illustrate that their density is substantially higher in the vicinity of the voids, suggesting that plasticity is severely localized. A larger scale EBSD map, shown in the inset of Fig. 4E, indicates that there are profuse voids surrounding the spall plane (dark-contrasted fracture plane). Many voids are identified at the grain boundaries, as they represent weak spots during dynamic tensile loading; these are accordingly the preferred void nucleation sites. However, numerous small voids are visible in the grains, especially where profuse deformation-induced interfaces emerge (fig. S4A). A rough statistical analysis (fig. S4B) of the size distribution of the voids indicates that voids located in the vicinity of the grain boundaries (yellow) are generally bigger than the ones formed within the grain interiors (blue) and are thus more susceptible to coalescence (i.e., for void size larger than 20 μm).

Failure mechanisms at high strain rates

Spalling generally occurs during the shock wave release and is a common failure mechanism of materials under impact loading. It is relatively well accepted that spalling can take place in ductile metals via void nucleation, growth, and coalescence. The detailed mechanisms, however, vary across different materials and depend heavily on the chemical composition, initial microstructure, and prior history of thermomechanical treatments. In the present study on CrCoNi, to characterize the microstructure adjacent to the voids, large-scale cross-sectional focused ion beam (FIB) was used to trench a 20-μm-long lamella located next to the spall plane; this permitted the use of electron microscopy to discern the precise details of the failure mechanisms related to void growth.

It is reasonable to postulate that voids nucleate from the pre-existing free volume of the material, including grain boundaries and vacancies. These defects are inevitable in pristine polycrystalline solids. In the current study involving energetic shock loading of CrCoNi, the sample was compressed first, which results in an increase in the defect population. Because of the low SFE of this alloy [~20 mJ/mm^2; (52)], the defect accumulation rate far exceeds that of annihilation, which results in a high density of defects whose spatial distribution play an important role in the void nucleation. Specifically, a higher GND density was observed in the vicinity of the grain boundaries (particularly annealing twin boundaries) as compared to the grain interiors (fig. S5). Because the generation of dislocations is also associated with vacancy production, a high GND density provides more nucleation sites, and, for this reason, most voids are observed not only at the grain boundaries but also in their close vicinity.

The nucleated voids tend to grow rapidly under extreme tensile loading. Huang *et al.* (36) investigated this phenomenon and concluded that void growth can be markedly accelerated above a critical stress. In an extreme strain rate laser-shock experiment where the stress level is in the range of tens of GPa, all voids are expected to grow, even over nanosecond time scales. Void growth naturally also depends sensitively on the stress triaxiality (45, 53); it has been shown that voids prefer to grow an equiaxial manner until impingement under high triaxiality stress states, whereas simultaneous smearing and growth of voids (void sheet mechanism) usually occurs with low triaxiality loading (35), the latter often being accompanied by the shear band formation. A similar phenomenon is observed in high-strength steels, where larger initial voids, formed at inclusions, link up in shear by void sheet coalescence
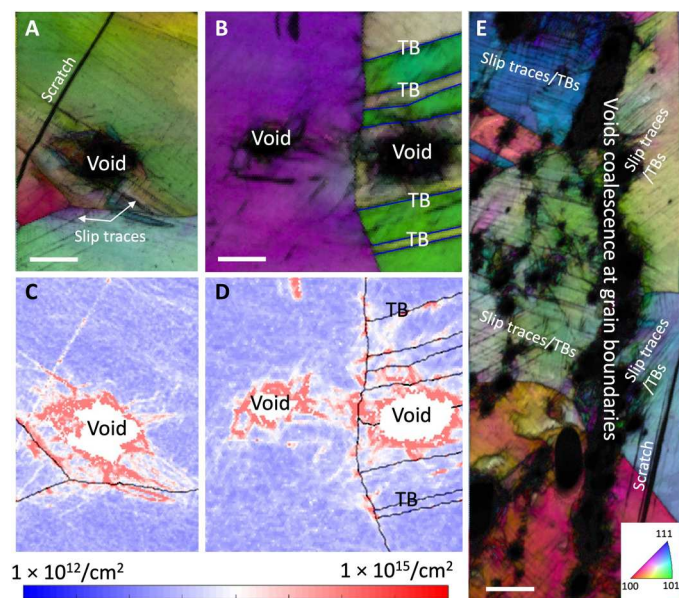
Fig. 4. Spatial distribution of the voids in the vicinity of spall plane. (**A**) Inverse pole figure mapping illustrates an individual void adjacent to a grain-boundary triple junction. (**B**) A pair of voids in the two neighboring grains: (left) located in the grain interior and (right) sandwiched between twin boundaries (TBs). (**C** and **D**) Geometrical necessary dislocations mapping indicates plasticity is localized in the vicinity of the voids. (**E**) Evidence of void coalescence, primarily at the grain boundaries. Smaller voids can be observed in the grain interiors with profuse slip traces in their vicinity. Scale bars, 10 μm.

involving smaller voids formed at the carbide particles (*54*). Our postmortem cross-sectional FIB experiment suggests the co-existence of both these void growth mechanisms for the shock loading of CrCoNi; the left-hand side of Fig. 5A confirms a few individual voids just before the impingement, whereas the center part of this figure highlights the shear-driven unstable growth of voids into microcracks. TEM micrographs adjacent to the voids (Fig. 5B) suggest that there exists a higher density of planar defects (stacking faults and nanotwins), indicating localized plasticity accompanied by void growth.

Void growth can be complicated by thermal softening as it is inevitably coupled with heat generation induced by the shock compression. Considering the extremely short time scale of the laser shock, i.e., 10s of ns, and relatively low thermal conductivity of HEAs, one can assume that adiabatic conditions prevail during void growth. This leads to the heterogeneous rise in temperature at the "hot spots." Therefore, the resultant microstructure around the voids after the passage of shock and release waves would likely be subjected to a delayed annealing process. Our TEM observations in Fig. 5C confirmed this hypothesis. The grain structure in the vicinity of the voids was seen to be severely refined and displayed little crystallographic relationship with the surrounding grains. This is attributed to recrystallization of the heavily deformed material at the locally elevated temperature. The transient nature of laser-shock experiments renders a limited recrystallization time, which leads to a nanocrystalline grain structure. Adjacent to the voids, a local temperature increase was estimated to be on the order of two times the average temperature of the sample, leading to local recrystallization (fig. S6). Note that the interaction and

recombination of defects can also lead to reorientation of the grain, also contributing to the recrystallization. Furthermore, strong shear localization occurs when the thermal softening dominates, which, in turn, generates additional sources of heat generation. Once shear localization is initiated, the degree of stress triaxiality is reduced markedly such that the voids grow collectively within the shear plane and rapidly develop into microcracks, as shown in Fig. 5A.

Effects of interfaces and plasticity on the void growth

It has been demonstrated that individual voids can expand by the emission of dislocation loops from the surface of the cavity (*33*, *40*, *44*). This mechanism was confirmed by our MD simulations for the CrCoNi MEA, where it is evident that when the triaxial stress reached a critical value, the void starts to grow with multiple dislocation loops emitted from the void surface. A high density of dislocations is generated, which moves away from the void surface by glide during dynamic tensile loading. The mean free path of these dislocations is constrained by the spatial dimension of the interfaces, which, to a large degree, determines the final geometry of the voids. Because a profuse array of planar defects, i.e., stacking faults, nanotwins, and hcp nanolamella, are generated before void nucleation during shock wave loading, it is reasonable to assume that they serve to constrain the growth of the voids. To verify this assumption and investigate the influence of planar defects created during shock compression on subsequent void growth, additional MD simulations on nanometer-sized void growth were carried out. On the basis of the experimental observation, evenly spaced stacking faults and nanotwins were introduced into the simulation cells before void growth. A single-crystal sample without any planar defects was also analyzed to serve as a reference.

Figure 6A illustrates the evolution of anisotropic void growth for the two cases, namely, an initially defect-free cell and a cell with twin boundaries. Exemplary void shapes are given in Fig. 6 (B and C). In the planar defect–free sample (Fig. 6B), the void grows uniformly because the dislocation loops emitted from voids are free from constraint. However, with the introduction of evenly spaced {111} nanotwins (Fig. 6C), they can effectively block the glide of these dislocation loops; this accordingly influences void growth in the [111] direction such that the final void geometry becomes penny-shaped due to the confinement by the initial twin boundaries (further details can be seen in movies S2 and S3). Figure 6D shows the corresponding dislocation density distribution along the [111] direction during void growth for both cells: the defect-free cell and the one containing nanotwins. It is clear that the emitted dislocation density is homogeneous in the defect-free cell, whereas there is a high dislocation density along the twin boundaries in the other cell due to dislocation-twin boundary interactions (*55*–*57*). The simulations further confirm that stacking faults can also influence the growth of voids, although they are not as effective as twin boundaries, as shown in Fig. 6A. For plasticity-controlled void growth, the volumetric growth rate of the void is mainly proportional to the applied volume strain rate regardless of the detailed microstructure (*58*). However, because plastic strain is created by dislocation emission from the void surface, our MD simulations demonstrate that microstructure does remarkably influence the slip path of the emitted dislocations to change the final shape of the voids, which would certainly act to influence their coalescence. To support this hypothesis, additional simulations of void
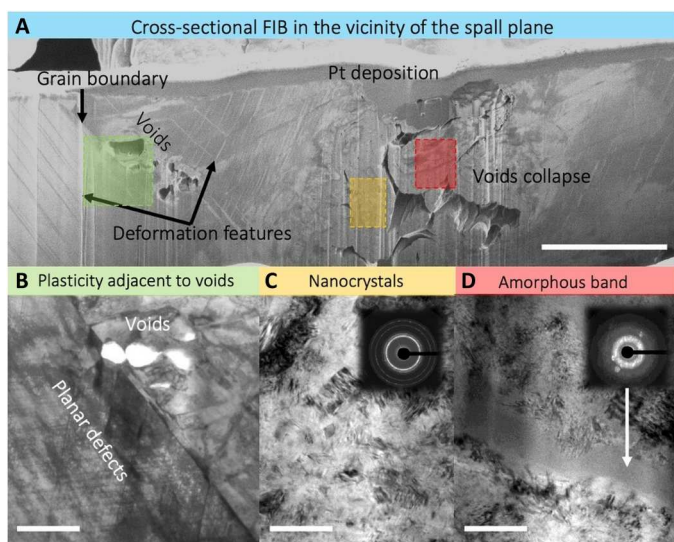
Fig. 5. Extreme deformation mechanisms adjacent to the voids. (**A**) Cross-sectional FIB image in the vicinity of the spall plane reveals several microvoids along the grain boundaries. Some microcracks, potentially resulted from void coalescence, were also observed. (**B**) TEM bright-field micrographs indicate that there exists a high density of planar defects adjacent to the voids. (**C**) Voids coalescence leads to severe plastic deformation, which largely refines the initially coarse-grained materials. The grain size can be as small as a few tens of nanometers, and, in some extreme cases, (**D**) amorphous band can be observed. Scale bars, 5 μm (A), 500 nm (B), and 100 nm (C) and (D). All the TEM samples are taken near the spall plane (rear surface) as shown schematically in Fig. 1C.

coalescence were conducted, specifically involving two initial voids being created in the cells without and with initial twin boundaries; the loading condition was held to be similar to the previous simulations. Figure 6 (E and F) displays the final configurations of the coalesced voids at same applied volumetric strain. In the planar defect–free sample (Fig. 6E), the two voids have grown and are about to coalesce to form a larger void; however, in the sample with nanotwins (Fig. 6F), due to the interaction between the twin boundaries and the dislocation, which results in anisotropic void growth, the coalescence of the voids is delayed such that the two voids remain separated (details are shown in movies S4 and S5). The simplified MD models reveal that although the total volume of the voids remains similar, the pre-existence of planar defects (stacking faults, twins and hexagonal lamella) introduced by shock compression can serve to delay the coalescence of certain voids that generate enhanced spall strength and damage tolerance under dynamic tension conditions.

Amorphization
Note that amorphous regions were also observed in the vicinity of the shear-localized regions (Fig. 5D). They are likely to be formed by the accumulation of defects, which leads to an increase in free energy of the crystalline lattice when the local defect density (ρ_d) is sufficiently high (26, 59)

$$E_{\text{lattice}}(T) + \frac{1}{2}\rho_d G b^2 > E_{\text{amorp}}(T) \qquad (2)$$

where E_{lattice} and E_{amorp} are the free energy of the crystalline and amorphous phases, respectively, G is the shear modulus, b is the

magnitude of the Burgers vector of the dislocations, and $\frac{1}{2}\rho_d G b^2$ is approximately the stored elastic energy induced by the defects. This corroborates with the previously reported phenomenon of mechanically induced solid-state amorphization in HEAs (60, 61).

Our MD simulations (Fig. 3F and fig. S7) indicate that the crystalline-to-amorphous phase transition preferably occurs in heavily deformed regions where multiple stacking faults and nanotwins interact with each other. Temperature rise produced by the shock compression is also estimated and shown in fig. S7A; however, as the temperature within the amorphous region is increased, it is well below the melting point of the alloy and thus confirms the solid-state nature of the phase transition. The radial distribution function of the region containing the amorphous phase was calculated and compared with the pure crystalline phase (i.e., with the sample at the same temperature but in the absence of mechanical loading); this indicated a much-reduced peak intensity starting from the second nearest neighbor, which confirms the disordered nature of the transformed materials.

The formation of the amorphous domains increases the strain energy absorption before fracture and thus provides an additional energy dissipation mechanism during impact loading of the CrCoNi-based HEA (26, 62). On the other hand, the appearance of the amorphous phase may reduce the spall resistance of the materials as voids would nucleate preferentially in these domains (63). This is still somewhat of an open question as the specific effect of amorphization on the mechanical behavior of the materials is still much in debate.

General remarks on HEAs subjected to high strain rate loading
We schematically summarize the deformation and failure of this MEA when subjected to very high strain rate laser-shock experiments in Fig. 7. The material is initially plastically deformed by a strong compressive wave, leaving a high density of defects behind the shock front. These defects usually comprise planar faults such as stacking faults, twins, and hexagonal lamella, leading to a 3D nanointerface network. In addition, there are profuse geometrically necessary dislocations generated along these nanointerfaces. Subsequently, upon shock wave release, the stress state becomes tensile with the result that the material undergoes void nucleation, growth, and coalescence, leading to outright failure. The compression-induced nanointerfaces play a vital role in the failure of the alloy in tension, as they confine the geometry and redistribute the nucleation of the voids. These mechanisms can ultimately improve the spall strength and damage tolerance of the material and lead to an excellent impact resistance of the MEA under strong shock conditions.

Compared with the longer pulse gas gun experiments (64), pulsed laser-driven shock experiment provides a higher magnitude of stress (tens to thousands of GPa versus several to tens of GPa) and strain rate (10^7 to 10^8/s versus 10^5 to 10^6/s), which consequently leads to higher defect generation and storage in compression. This can explain a substantial rate dependence of spall strength of the CrCoNi-based HEAs when measured by various techniques such as gas gun and pulsed laser-driven shock compression. We summarize the dynamic behavior of CrCoNi-containing HEAs in fig. S8; most of the alloys express similar strain hardenability at elevated strain rates, indicating their excellent mechanical properties under extreme conditions (22, 23, 25, 65–72). Note that the
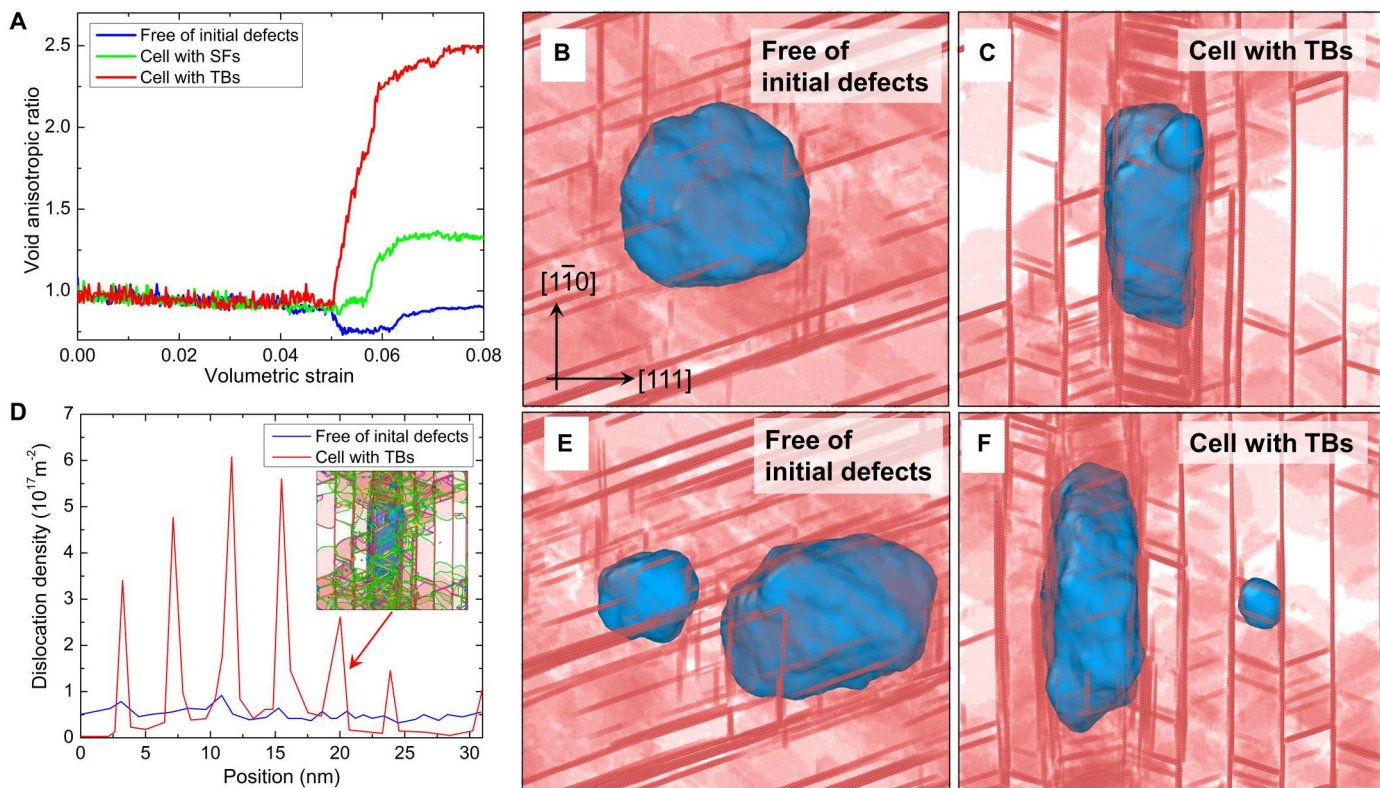
Fig. 6. MD simulations of nanometer-sized void growth and coalescence in the CrCoNi MEA with different microstructures. (**A**) Anisotropic ratio of the single void growth during loading. The blue line represents void growth in a single crystalline sample free of planar defects, the green line represents void growth in a sample with evenly spaced SFs, and the red line represents void growth in a sample with evenly spaced twin boundaries. Final shape of the void (blue represents the void surface atoms, and red represents the hcp atoms) for (**B**) the sample without initial defects and (**C**) the sample with evenly spaced twin boundaries. (**D**) Dislocation density distribution in the simulation cell in [111] direction. Inset corresponds to the cell with twin boundaries (red curve). Green lines in the inset represents partial dislocation lines. (**E**) Voids grow without pre-existing twin boundaries and with pre-existing twin boundary (**F**). For the visualization, hcp atoms are colored in red and void surface atoms are colored in blue, with all the other types of atoms set to be invisible.

deformation and failure mechanisms demonstrated here are not necessarily unique to HEAs but rather to fcc metals and alloys with a low SFE (which of course includes many fcc MEA/HEAs). For example, some austenitic steels (e.g., 304 and 316 stainless) can achieve a dynamic strength that is as high, if not higher than, the CrCoNi MEA (*25*). These alloys are also chemically complex owing to the similar choice of alloying elements to the fcc HEAs. Therefore, the detailed mechanisms in terms of the interaction between the complex local chemical environment and the defect dynamics relevant to the damage accumulation should be similar in these alloys. It should also be noted that HEAs usually contain short range order (*48*, *73–78*), the degree of which depends heavily on the thermomechanical history of the specimen, which is also likely to affect the dynamic behavior of the material (*79*). Nevertheless, our experiments and MD simulations subject the CrCoNi MEA to extremely high strain rates and provide evidence and rationale on the sound impact resistance of the alloy. Higher strain rate of the pulsed laser technique favors athermal deformation modes such as twinning and deviatoric phase transition. If used properly, pulsed laser can also be applied to introduce beneficial compressive residual strain field in alloys. Further improvement in impact resistance may be obtained by tailoring the SFE of these materials to promote TWIP, TRIP, and amorphization effects (*80*).

MATERIALS AND METHODS
Preprocessing of the materials
The as-received material was a pristine, equiatomic, single-phase CrCoNi MEA, cold rolled with reduction in thickness of 80%. It was then annealed at 1000°C for 48 hours to reduce the deformation-induced defects and recrystallize the alloy. After annealing, recrystallization and grain growth resulted in a nominally equiaxed grain size of ~100 µm. Because of the coarse grain size, the alloy exhibited a relatively low tensile yield strength of ~200 MPa at ambient temperatures (*48*), but the sequence of deformation mechanisms inherent in this MEA leads to continuous strain hardening. The longitudinal (c_l) and transverse (c_s) sound velocities were measured by pulse-echo ultrasonic method with c_l = 6 km/s and c_s = 3.26 km/s. The bulk sound speed was calculated to be c_b = 4.67 km/s.

Laser-shock experiments
Laser-shock experiments were conducted at the Omega laser facility, Laboratory of Laser Energetics, University of Rochester. The 352-nm wavelength laser with a nominal square pulse shape and duration of 1 ns was focused (into a spot size of 3 mm in diameter) onto the target package, which consisted of a 20-µm polystyrene ablator, followed by the actual target. For the three VISAR experiments, MEA foils (100 µm thick) were shocked using laser energies
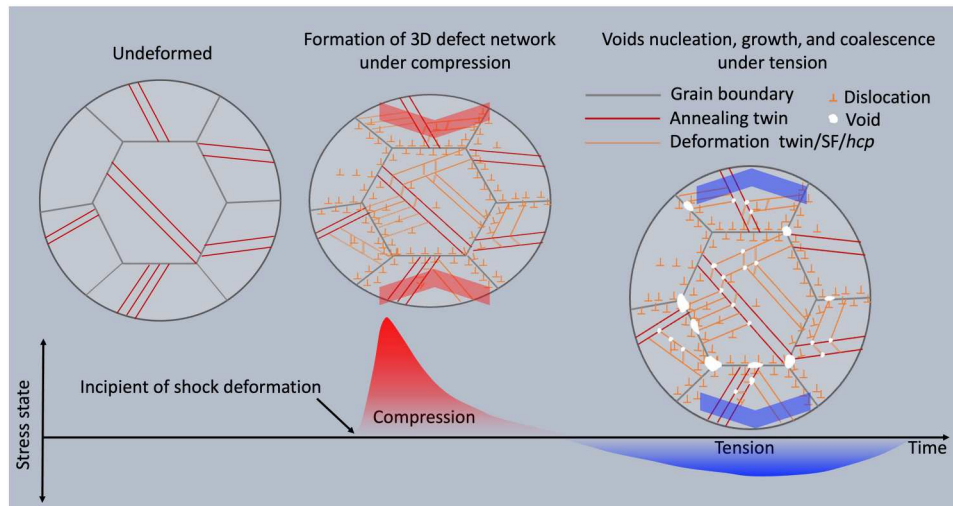
Fig. 7. Schematic illustration of the microstructure of the CrCoNi MEA during the laser-shock experiment. The material was first compressed along the direction of shock wave propagation. A 3D network of defects and nanointerfaces forms on {111} planes, including annealing twins, stacking faults and hcp lamella initiated from the grain boundaries, secondary defects between primary ones, and geometrically necessary dislocations enriched at the grain boundaries. The same material was then subjected to a tensile stress, which leads to voids nucleation, growth, and coalescence. Many voids are located at the grain boundaries due to their intrinsically lower strength than the grain interior. In addition, various voids emerged in regions where the compression-induced planar defects created more nucleation sites for void nucleation.

between 100 and 150 J, yielding a nominal ablation pressure (P_{ab}) between 100 and 130 GPa using Lindl's scaling law (*81*), viz

$$P_{ab} \approx 40 \left(\frac{I}{\lambda} \right)^{\frac{2}{3}}$$

where I is the laser intensity and λ is the laser wavelength. For recovery experiments, thicker samples (2 mm) were placed behind the thin foil. Similar laser energies were applied to the samples to examine the microstructure from the compression side. Much higher laser energies (two laser beams, each of which had a nominal laser energy of 450 J) were used to cause spallation near the rear surface of the sample and to characterize the deformed microstructure.

Microstructural characterization
Multiscale deformation microstructures were examined. First, cross-sectional EBSD measurements were conducted to identify the microstructural gradient along the direction of shock wave propagation. In particular, we focused on the region in the vicinity of the fracture surface, which was located near the rear surface of the sample. The GND density, ρ_{GND}, is calculated by the following equation, which is commonly used in the literature (*82*)

$$\rho_{GND} = \frac{2\theta}{ub}$$

where b is the magnitude of the Burgers vector of full dislocation in the CrCoNi MEA, u is unit length of the measured area (the step size of the EBSD scan), and θ represents the local misorientation angle, which is approximated by the kernel average misorientation (less than 3°). FIB milling was used to extract electron transparent samples in the vicinity of the voids. TEM was used to characterize the deformation microstructure.

MD simulations
Two sets of MD simulations were conducted, including the non-equilibrium MD simulations of shock compression and simulations with nanometer-sized void growth induced in pre-existing micro-structures, containing twins and/or stacking faults. For the shock compression simulations, the shock waves were generated following the widely used piston-driven method (*83–85*), where a constant particle velocity U_p in shock compression direction was assigned to a thin slab of atoms in one end of the sample while the rest of the system was simulated under conditions represented by the constant-energy, constant-volume (NVE) microcanonical ensemble. The sample comprised the single-crystalline CrCoNi MEA containing around 3.84 million atoms and has a size of ~19 nm by 19 nm by 125 nm, with the shock direction oriented along the [110] direction. Periodic boundary conditions transverse to the shock direction were used. The sample was relaxed at temperature of 5 K for 30 ps and then followed by the piston drive. The piston velocity was increased linearly from zero to U_p = 1 km/s over 10 ps and then kept constant.

For the nanometer-sized void growth simulations, a cubic simulation cell was created with size of ~30 x 30 x 30 nm, with single crystalline structure containing stacking faults and/or nanotwins. One or two spherical voids with radius equal to 1.5 nm were created in the cell. Periodic boundary conditions were imposed in all directions. To model the tensile stress generated by the reflecting shock wave, a uniaxial tensile strain was applied to the sample in the [111] direction at a strain rate of 10^7 s^{-1} at a temperature of 500 K in a canonical ensemble with lateral strains impeded. The anisotropic ratio of the void was computed as $r = \frac{D_{112}+D_{110}}{2D_{111}}$, where D_{112}, D_{110}, D_{111} are the dimensions of the void in [112], [110], and [111] directions, respectively. All the MD simulations were performed using the software package LAMMPS (*86*) with the atomic configurations and dislocations post-processed and visualized through CAT (*87*)

and OVITO (*88*). The embedded atom model potential for CrCoNi was used to describe the interatomic interactions (*89*). Compared to ab initio calculations and experiments, this potential successfully matches the cohesive energies, lattice parameters, elastic constants, and phonon frequencies. Of importance to plasticity studies, the potential is well characterized in terms of the energetics of the stacking faults (*89*). Since its introduction, the potential has been extensively used for studying the CrCoNi alloy (*48*, *90–93*), including the effects of lattice distortion and chemical short-range order on the deformation mechanisms of the CrCoNi alloy under shock loading (*63*, *94*).

Supplementary Materials
This PDF file includes:
Figs. S1 to S8
Legends for movies S1 to S5

Other Supplementary Material for this manuscript includes the following:
Movies S1 to S5

REFERENCES AND NOTES

1. J.-W. Yeh, S.-K. Chen, S.-J. Lin, J.-Y. Gan, T.-S. Chin, T.-T. Shun, C.-H. Tsau, S.-Y. Chang, Nanostructured high-entropy alloys with multiple principal elements: Novel alloy design concepts and outcomes. *Adv. Eng. Mater.* **6**, 299–303 (2004).

2. B. Cantor, I. T. H. Chang, P. Knight, A. J. B. Vincent, Microstructural development in equiatomic multicomponent alloys. *Mater. Sci. Eng. A* **375–377**, 213–218 (2004).

3. O. N. Senkov, G. B. Wilks, D. B. Miracle, C. P. Chuang, P. K. Liaw, Refractory high-entropy alloys. *Intermetallics* **18**, 1758–1765 (2010).

4. Y. Zhang, T. T. Zuo, Z. Tang, M. C. Gao, K. A. Dahmen, P. K. Liaw, Z. P. Lu, Microstructures and properties of high-entropy alloys. *Prog. Mater. Sci.* **61**, 1–93 (2014).

5. Q. Pan, L. Zhang, R. Feng, Q. Lu, K. An, A. C. Chuang, J. D. Poplawsky, P. K. Liaw, L. Lu, Gradient cell–structured high-entropy alloy with exceptional strength and ductility. *Science* **374**, 984–989 (2021).

6. E. Ma, X. Wu, Tailoring heterogeneities in high-entropy alloys to promote strength–ductility synergy. *Nat. Commun.* **10**, 5623 (2019).

7. A. J. Zaddach, C. Niu, C. C. Koch, D. L. Irving, Mechanical properties and stacking fault energies of NiFeCrCoMn high-entropy alloy. *JOM* **65**, 1780–1789 (2013).

8. Z. Li, S. Zhao, R. O. Ritchie, M. A. Meyers, Mechanical properties of high-entropy alloys with emphasis on face-centered cubic alloys. *Prog. Mater. Sci.* **102**, 296–345 (2019).

9. Q. Ding, Y. Zhang, X. Chen, X. Fu, D. Chen, S. Chen, L. Gu, F. Wei, H. Bei, Y. Gao, M. Wen, J. Li, Z. Zhang, T. Zhu, O. Ritchie, Q. Yu, Tuning element distribution, structure and properties by composition in high-entropy alloys. *Nature* **574**, 223–227 (2019).

10. E. P. George, W. A. Curtin, C. C. Tasan, High entropy alloys: A focused review of mechanical properties and deformation mechanisms. *Acta Mater.* **188**, 435–474 (2020).

11. Z. Lei, X. Liu, Y. Wu, H. Wang, S. Jiang, S. Wang, X. Hui, Y. Wu, B. Gault, P. Kontis, D. Raabe, L. Gu, Q. Zhang, H. Chen, H. Wang, J. Liu, K. An, Q. Zeng, T.-G. Nieh, Z. Lu, Enhanced strength and ductility in a high-entropy alloy via ordered oxygen complexes. *Nature* **563**, 546–550 (2018).

12. Z. Zhang, H. Sheng, Z. Wang, B. Gludovatz, Z. Zhang, E. P. George, Q. Yu, S. X. Mao, R. O. Ritchie, Dislocation mechanisms and 3D twin architectures generate exceptional strength-ductility-toughness combination in CrCoNi medium-entropy alloy. *Nat. Commun.* **8**, 14390 (2017).

13. B. Gludovatz, A. Hohenwarter, D. Catoor, E. H. Chang, E. P. George, R. O. Ritchie, A fracture-resistant high-entropy alloy for cryogenic applications. *Science* **345**, 1153–1158 (2014).

14. Z. Li, K. Gokuldoss Pradeep, Y. Deng, D. Raabe, C. Cem Tasan, Metastable high-entropy dual-phase alloys overcome the strength-ductility trade-off. *Nature* **534**, 227–230 (2016).

15. F. Otto, A. Dlouhý, C. Somsen, H. Bei, G. Eggeler, E. P. George, The influences of temperature and microstructure on the tensile properties of a CoCrFeMnNi high-entropy alloy. *Acta Mater.* **61**, 5743–5755 (2013).

16. J. Su, D. Raabe, Z. Li, Hierarchical microstructure design to tune the mechanical behavior of an interstitial TRIP-TWIP high-entropy alloy. *Acta Mater.* **163**, 40–54 (2019).

17. C. Niu, C. R. LaRosa, J. Miao, M. J. Mills, M. Ghazisaeidi, Magnetically-driven phase transformation strengthening in high entropy alloys. *Nat. Commun.* **9**, 1363 (2018).

18. Z. Li, S. Zhao, H. Diao, P. K. Liaw, M. A. Meyers, High-velocity deformation of Al0.3CoCrFeNi high-entropy alloy: Remarkable resistance to shear failure. *Sci. Rep.* **7**, 42742 (2017).

19. Z. Li, S. Zhao, S. M. Alotaibi, Y. Liu, B. Wang, M. A. Meyers, Adiabatic shear localization in the CrMnFeCoNi high-entropy alloy. *Acta Mater.* **151**, 424–431 (2018).

20. Z. Yang, M. Yang, Y. Ma, L. Zhou, W. Cheng, F. Yuan, X. Wu, Strain rate dependent shear localization and deformation mechanisms in the CrMnFeCoNi high-entropy alloy with various microstructures. *Mater. Sci. Eng. A* **793**, 139854 (2020).

21. X. Wu, M. Yang, P. Jiang, C. Wang, L. Zhou, F. Yuan, E. Ma, Deformation nanotwins suppress shear banding during impact test of CrCoNi medium-entropy alloy. *Scr. Mater.* **178**, 452–456 (2020).

22. Y. Yang, S. Yang, H. Wang, Effects of the phase content on dynamic damage evolution in Fe50Mn30Co10Cr10 high entropy alloy. *J. Alloys Compd.* **851**, 156883 (2021).

23. Z. J. Jiang, J. Y. He, H. Y. Wang, H. S. Zhang, Z. P. Lu, L. H. Dai, J. Y. He, H. Y. Wang, H. S. Zhang, Z. P. Lu, L. H. Dai, Shock compression response of high entropy alloys. *Mater. Res. Lett.* **4**, 226–232 (2016).

24. Z.-C. Xie, C. Li, H.-Y. Wang, C. Lu, L.-H. Dai, Hydrogen induced slowdown of spallation in high entropy alloy under shock loading. *Int. J. Plast.* **139**, 102944 (2021).

25. N. B. Zhang, J. Xu, Z. D. Feng, Y. F. Sun, J. Y. Huang, X. J. Zhao, X. H. Yao, S. Chen, L. Lu, S. N. Luo, Shock compression and spallation damage of high-entropy alloy Al0.1CoCrFeNi. *J. Mater. Sci. Technol.* **128**, 1–9 (2022).

26. S. Zhao, Z. Li, C. Zhu, W. Yang, Z. Zhang, D. E. J. Armstrong, P. S. Grant, R. O. Ritchie, M. A. Meyers, Amorphization in extreme deformation of the CrMnFeCoNi high-entropy alloy. *Sci. Adv.* **7**, eabb3108 (2021).

27. M. A. Meyers, *Dynamic Behavior of Materials* (John Wiley & Sons, 1994).

28. J. Belak, On the nucleation and growth of voids at high strain-rates. *J. Comput. Aided Mater. Des.* **5**, 193–206 (1998).

29. X. Y. Wu, K. T. Ramesh, T. W. Wright, The effects of thermal softening and heat conduction on the dynamic growth of voids. *Int. J. Solids Struct.* **40**, 4461–4478 (2003).

30. G. I. Kanel, A. S. Savinykh, G. V. Garkushin, S. V. Razorenov, Effects of temperature and strain on the resistance to high-rate deformation of copper in shock waves. *J. Appl. Phys.* **128**, 115901 (2020).

31. X. Y. Wu, K. T. Ramesh, T. W. Wright, The dynamic growth of a single void in a viscoplastic material under transient hydrostatic loading. *J. Mech. Phys. Solids* **51**, 1–26 (2003).

32. X. Huang, Z. Ling, L. H. Dai, Cavitation instabilities in bulk metallic glasses. *Int. J. Solids Struct.* **50**, 1364–1372 (2013).

33. V. A. Lubarda, M. S. Schneider, D. H. Kalantar, B. A. Remington, M. A. Meyers, Void growth by dislocation emission. *Acta Mater.* **52**, 1397–1408 (2004).

34. D. Curran, Dynamic failure of solids. *Phys. Rep.* **147**, 253–388 (1987).

35. V. Tvergaard, Influence of voids on shear band instabilities under plane strain conditions. *Int. J. Fract.* **17**, 389–407 (1981).

36. Y. Huang, J. W. Hutchinson, V. Tvergaard, Cavitation instabilities in elastic-plastic solids. *J. Mech. Phys. Solids* **39**, 223–241 (1991).

37. J. W. Wilkerson, K. T. Ramesh, A dynamic void growth model governed by dislocation kinetics. *J. Mech. Phys. Solids* **70**, 262–280 (2014).

38. J. W. Wilkerson, K. T. Ramesh, Unraveling the anomalous grain size dependence of cavitation. *Phys. Rev. Lett.* **117**, 215503 (2016).

39. M. A. Meyers, H. Jarmakani, E. M. Bringa, B. A. Remington, Dislocations in Shock Compression and Release, in *Dislocations in Solids* (Chapter 89., 2009), pp. 91–197.

40. T. P. Remington, E. N. Hahn, S. Zhao, R. Flanagan, J. C. E. Mertens, S. Sabbaghianrad, T. G. Langdon, C. E. Wehrenberg, B. R. Maddox, D. C. Swift, B. A. Remington, N. Chawla, M. A. Meyers, Spall strength dependence on grain size and strain rate in tantalum. *Acta Mater.* **158**, 313–329 (2018).

41. G. Righi, C. J. Ruestes, C. v. Stan, S. J. Ali, R. E. Rudd, M. Kawasaki, H.-S. Park, M. A. Meyers, Towards the ultimate strength of iron: Spalling through laser shock. *Acta Mater.* **215**, 117072 (2021).

42. A. G. Perez-Bergquist, E. K. Cerreta, C. P. Trujillo, F. Cao, G. T. Gray III, Orientation dependence of void formation and substructure deformation in a spalled copper bicrystal. *Scr. Mater.* **65**, 1069–1072 (2011).

43. S. J. Fensin, J. P. Escobedo-Diaz, C. Brandl, E. K. Cerreta, G. T. Gray III, T. C. Germann, S. M. Valone, Effect of loading direction on grain boundary failure under shock loading. *Acta Mater.* **64**, 113–122 (2014).

44. R. E. Rudd, J. F. Belak, Void nucleation and associated plasticity in dynamic fracture of polycrystalline copper: An atomistic simulation. *Comput. Mater. Sci.* **24**, 148–153 (2002).

45. C. McVeigh, F. Vernerey, W. K. Liu, B. Moran, G. Olson, An interactive micro-void shear localization mechanism in high strength steels. *J. Mech. Phys. Solids* **55**, 225–244 (2007).

46. Y. Tang, D. Y. Li, Dynamic response of high-entropy alloys to ballistic impact. *Sci. Adv.* **8**, eabp9096 (2022).

47. Z. Xie, W.-R. Jian, S. Xu, I. J. Beyerlein, X. Zhang, Z. Wang, X. Yao, Role of local chemical fluctuations in the shock dynamics of medium entropy alloy CoCrNi. *Acta Mater.* **221**, 117380 (2021).

48. R. Zhang, S. Zhao, J. Ding, Y. Chong, T. Jia, C. Ophus, M. Asta, R. O. Ritchie, A. M. Minor, Short-range order and its impact on the CrCoNi medium-entropy alloy. *Nature* **581**, 283–287 (2020).

49. Y. H. Zhang, Y. Zhuang, A. Hu, J. J. Kai, C. T. Liu, The origin of negative stacking fault energies and nano-twin formation in face-centered cubic high entropy alloys. *Scr. Mater.* **130**, 96–99 (2017).

50. J. Miao, C. E. Slone, T. M. Smith, C. Niu, H. Bei, M. Ghazisaeidi, G. M. Pharr, M. J. Mills, The evolution of the deformation substructure in a Ni-Co-Cr equiatomic solid solution alloy. *Acta Mater.* **132**, 35–48 (2017).

51. L. A. Zepeda-Ruiz, A. Stukowski, T. Oppelstrup, Bulatov, Probing the limits of metal plasticity with molecular dynamics simulations. *Nature* **550**, 492–495 (2017).

52. G. Laplanche, A. Kostka, C. Reinhart, J. Hunfeld, G. Eggeler, E. P. George, Reasons for the superior mechanical properties of medium-entropy CrCoNi compared to high-entropy CrMnFeCoNi. *Acta Mater.* **128**, 292–303 (2017).

53. J. R. Rice, D. Tracey, On the ductile enlargement of voids in triaxial stress fields. *J. Mech. Phys. Solids* **17**, 201–217 (1969).

54. T. B. Cox, J. R. Low, An investigation of the plastic fracture of AISI 4340 and 18 Nickel-200 grade maraging steels. *Metall. Trans.* **5**, 1457–1470 (1974).

55. S.-W. Kim, X. Li, H. Gao, S. Kumar, In situ observations of crack arrest and bridging by nanoscale twins in copper thin films. *Acta Mater.* **60**, 2959–2972 (2012).

56. Q. Qin, S. Yin, G. Cheng, X. Li, T.-H. Chang, G. Richter, Y. Zhu, H. Gao, Recoverable plasticity in penta-twinned metallic nanowires governed by dislocation nucleation and retraction. *Nat. Commun.* **6**, 5983 (2015).

57. G. Cheng, S. Yin, C. Li, T.-H. Chang, G. Richter, H. Gao, Y. Zhu, *In-situ* TEM study of dislocation interaction with twin boundary and retraction in twinned metallic nanowires. *Acta Mater.* **196**, 304–312 (2020).

58. J. Lian, M. Suery, Effect of strain rate sensitivity and cavity growth rate on failure of superplastic material. *Mater. Sci. Technol.* **2**, 1093–1098 (1986).

59. S. Zhao, B. Li, B. A. Remington, C. E. Wehrenberg, H. S. Park, E. N. Hahn, M. A. Meyers, Directional amorphization of covalently-bonded solids: A generalized deformation mechanism in extreme loading. *Mater. Today* **49**, 59–67 (2021).

60. H. Wang, D. Chen, X. An, Y. Zhang, S. Sun, Y. Tian, Z. Zhang, A. Wang, J. Liu, M. Song, S. P. Ringer, T. Zhu, X. Liao, Deformation-induced crystalline-to-amorphous phase transformation in a CrMnFeCoNi high-entropy alloy. *Sci. Adv.* **7**, eabe3105 (2021).

61. K. Ming, W. Lu, Z. Li, X. Bi, J. Wang, Amorphous bands induced by low temperature tension in a non-equiatomic CrMnFeCoNi alloy. *Acta Mater.* **188**, 354–365 (2020).

62. K. Jiang, Q. Zhang, J. Li, X. Li, F. Zhao, B. Hou, T. Suo, Abnormal hardening and amorphization in an FCC high entropy alloy under extreme uniaxial tension. *Int. J. Plast* **159**, 103463 (2022).

63. W.-R. Jian, Z. Xie, S. Xu, X. Yao, I. J. Beyerlein, Shock-induced amorphization in medium entropy alloy CoCrNi. *Scr. Mater.* **209**, 114379 (2022).

64. M. C. Hawkins, S. Thomas, R. S. Hixson, J. Gigax, N. Li, C. Liu, J. A. Valdez, S. Fensin, Dynamic properties of FeCrMnNi, a high entropy alloy. *Mater. Sci. Eng. A* **840**, 142906 (2022).

65. D. Thürmer, S. Zhao, O. R. Deluigi, C. Stan, I. A. Alhafez, H. M. Urbassek, M. A. Meyers, E. M. Bringa, N. Gunkelmann, Exceptionally high spallation strength for a high-entropy alloy demonstrated by experiments and simulations. *J. Alloys Compd.* **895**, 162567 (2022).

66. K. Shi, J. Cheng, L. Cui, J. Qiao, J. Huang, M. Zhang, H. Yang, Z. Wang, Ballistic impact response of Fe$_{40}$Mn$_{20}$Cr$_{20}$Ni$_{20}$ high-entropy alloys. *J. Appl. Phys.* **132**, 205105 (2022).

67. K. Wang, X. Jin, Y. Zhang, P. K. Liaw, J. Qiao, Dynamic tensile mechanisms and constitutive relationship in CrFeNi medium entropy alloys at room and cryogenic temperatures. *Phys. Rev. Mater.* **5**, 113608 (2021).

68. S. P. Zhao, Z. D. Feng, L. X. Li, X. J. Zhao, L. Lu, S. Chen, N. B. Zhang, Y. Cai, S. N. Luo, Dynamic mechanical properties, deformation and damage mechanisms of eutectic high-entropy alloy AlCoCrFeNi21 under plate impact. *J. Mater. Sci. Technol.* **134**, 178–188 (2023).

69. K. Ren, H. Liu, R. Chen, Y. Tang, B. Guo, S. Li, J. Wang, R. Wang, F. Lu, Compression properties and impact energy release characteristics of TiZrNbV high-entropy alloy. *Mater. Sci. Eng. A* **827**, 142074 (2021).

70. A. Fu, B. Liu, Z. Li, B. Wang, Y. Cao, Y. Liu, Dynamic deformation behavior of a FeCrNi medium entropy alloy. *J. Mater. Sci. Technol.* **100**, 120–128 (2022).

71. J. C. Cheng, J. Xu, X. J. Zhao, K. W. Shi, J. Li, Q. Zhang, J. W. Qiao, J. Y. Huang, S. N. Luo, Shock compression and spallation of a medium-entropy alloy Fe$_{40}$Mn$_{20}$Cr$_{20}$Ni$_{20}$. *Mater. Sci. Eng. A* **847**, 143311 (2022).

72. Z. Wang, T. Zhang, E. Tang, R. Xiong, Z. Jiao, J. Qiao, Formation and deformation mechanisms in gradient nanostructured NiCoCrFe high entropy alloys upon supersonic impacts. *Appl. Phys. Lett.* **119**, 201901 (2021).

73. P. Singh, A. V. Smirnov, D. D. Johnson, Atomic short-range order and incipient long-range order in high-entropy alloys. *Phys. Rev. B.* **91**, 224204 (2015).

74. Y. Ma, Q. Wang, C. Li, L. J. Santodonato, M. Feygenson, C. Dong, P. K. Liaw, Chemical short-range orders and the induced structural transition in high-entropy alloys. *Scr. Mater.* **144**, 64–68 (2018).

75. T. Kostiuchenko, A. V. Ruban, J. Neugebauer, A. Shapeev, F. Körmann, Short-range order in face-centered cubic VCoNi alloys. *Phys. Rev. Mater.* **4**, 113802 (2020).

76. F. X. Zhang, S. Zhao, K. Jin, H. Xue, G. Velisa, H. Bei, R. Huang, J. Y. P. Ko, D. C. Pagan, J. C. Neuefeind, W. J. Weber, Y. Zhang, Local structure and short-range order in a NiCoCr solid solution alloy. *Phys. Rev. Lett.* **118**, 205501 (2017).

77. Y. Wu, F. Zhang, X. Yuan, H. Huang, X. Wen, Y. Wang, M. Zhang, H. Wu, X. Liu, H. Wang, S. Jiang, Z. Lu, Short-range ordering and its effects on mechanical properties of high-entropy alloys. *J. Mater. Sci. Technol.* **62**, 214–220 (2021).

78. X. Chen, Q. Wang, Z. Cheng, M. Zhu, H. Zhou, P. Jiang, L. Zhou, Q. Xue, F. Yuan, J. Zhu, X. Wu, E. Ma, Direct observation of chemical short-range order in a medium-entropy alloy. *Nature* **592**, 712–716 (2021).

79. A. Gupta, W.-R. Jian, S. Xu, I. J. Beyerlein, G. J. Tucker, On the deformation behavior of CoCrNi medium entropy alloys: Unraveling mechanistic competition. *Int. J. Plast.* **159**, 103442 (2022).

80. Y. Z. Wang, Z. M. Jiao, G. B. Bian, H. J. Yang, H. W. He, Z. H. Wang, P. K. Liaw, J. W. Qiao, Dynamic tension and constitutive model in Fe$_{40}$Mn$_{20}$Cr$_{20}$Ni$_{20}$ high-entropy alloys with a heterogeneous structure. *Mater. Sci. Eng. A* **839**, 142837 (2022).

81. J. Lindl, Development of the indirect-drive approach to inertial confinement fusion and the target physics basis for ignition and gain. *Phys. Plasmas* **2**, 3933 (1995).

82. M. Calcagnotto, D. Ponge, E. Demir, D. Raabe, Orientation gradients and geometrically necessary dislocations in ultrafine grained dual-phase steels studied by 2D and 3D EBSD. *Mater. Sci. Eng. A* **527**, 2738–2746 (2010).

83. N. Gunkelmann, E. M. Bringa, H. M. Urbassek, Influence of phase transition on shock-induced spallation in nanocrystalline iron. *J. Appl. Phys.* **118**, 185902 (2015).

84. E. N. Hahn, T. C. Germann, R. J. Ravelo, J. E. Hammerberg, M. A. Meyers, Non-equilibrium molecular dynamics simulations of spall in single crystal tantalum. *AIP Conf. Proc.* **1793**, 070006 (2017).

85. N. Gunkelmann, E. M. Bringa, D. R. Tramontina, C. J. Ruestes, M. J. Suggit, A. Higginbotham, J. S. Wark, H. M. Urbassek, Shock waves in polycrystalline iron: Plasticity and phase transitions. *Phys. Rev. B.* **89**, 140102(R) (2014).

86. S. Plimpton, Fast parallel algorithms for short-range molecular dynamics. *J. Comput. Phys.* **117**, 1–19 (1995).

87. A. Stukowski, V. V. Bulatov, A. Arsenlis, Automated identification and indexing of dislocations in crystal interfaces. *Modelling Simul. Mater. Sci. Eng.* **20**, 085007 (2012).

88. A. Stukowski, Visualization and analysis of atomistic simulation data with OVITO–the Open Visualization Tool. *Modelling Simul. Mat. Sci. Eng.* **18**, 015012 (2010).

89. Q.-J. Li, H. Sheng, E. Ma, Strengthening in multi-principal element alloys with local-chemical-order roughened dislocation pathways. *Nat. Commun.* **10**, 3563 (2019).

90. W.-R. Jian, Z. Xie, S. Xu, Y. Su, X. Yao, I. J. Beyerlein, Effects of lattice distortion and chemical short-range order on the mechanisms of deformation in medium entropy alloy CoCrNi. *Acta Mater.* **199**, 352–369 (2020).

91. W.-R. Jian, L. Wang, W. Bi, S. Xu, I. J. Beyerlein, Role of local chemical fluctuations in the melting of medium entropy alloy CoCrNi. *Appl. Phys. Lett.* **119**, 121904 (2021).

92. F. Cao, Y. Chen, S. Zhao, E. Ma, L. Dai, Grain boundary phase transformation in a CrCoNi complex concentrated alloy. *Acta Mater.* **209**, 116786 (2021).

93. F.-H. Cao, Y.-J. Wang, L.-H. Dai, Novel atomic-scale mechanism of incipient plasticity in a chemically complex CrCoNi medium-entropy alloy associated with inhomogeneity in local chemical environment. *Acta Mater.* **194**, 283–294 (2020).

94. M. Zhang, Q. Yu, C. Frey, F. Walsh, M. I. Payne, P. Kumar, D. Liu, T. M. Pollock, M. D. Asta, R. O. Ritchie, A. M. Minor, Determination of peak ordering in the CrCoNi medium-entropy alloy via nanoindentation. *Acta Mater.* **241**, 118380 (2022).

Acknowledgments